

## Photoelectron angular distributions from the subshells of high- $Z$ elements

Young Soon Kim and R. H. Pratt

*Department of Physics and Astronomy, University of Pittsburgh, Pittsburgh, Pennsylvania 15260*

Akiva Ron

*Racah Institute of Physics, Hebrew University of Jerusalem, Jerusalem, Israel*

H. K. Tseng

*Institute of Physics and Astronomy and Department of Physics, National Central University, Chung-Li, Taiwan, Republic of China*

(Received 17 March 1980)

Numerical predictions are obtained, within a relativistic multipole central-field approximation calculation, for the radial matrix elements and resulting angular distributions of photoelectrons ejected from inner through outer subshells of uranium and for photoelectron energies from near threshold (1 eV) to 100 keV. Some data are also presented for outer subshells of mercury. We confirm that for inner shells higher-multipole effects persist to low energies, while we find that for outer shells such effects become small. For uranium inner  $ns$  subshells the asymmetry parameter  $\beta_{ns}$  differs from its nonrelativistic value 2, but not more than 30% (for  $n < 4$ ), until the energy becomes quite high (the radial matrix elements for  $ns \rightarrow \epsilon p_{1/2}$  and  $ns \rightarrow \epsilon p_{3/2}$  transitions for these inner shells are similar). For outer  $s$  subshells relativistic spin-orbit splittings cause large deviations from the nonrelativistic predictions which can be understood from the magnitudes, zeros, and splittings of the two radial matrix elements. For U  $6p_{1/2}$  and  $6p_{3/2}$ ,  $\beta_{6p}$  has the same qualitative features found in nonrelativistic calculations for outer  $p$  shells of other high- $Z$  elements, but the angular distributions from the two states do differ in detail. Such differences in angular distributions of the photoelectrons from the two  $j$  substates of given  $l$  become smaller for inner  $p$  shells. For outer  $d$  and  $f$  subshells the asymmetry parameter oscillates with photoelectron energy in a manner similar to that found by Manson in nonrelativistic dipole  $d$ -subshell calculations, and no qualitatively important relativistic effects have been identified; this is due to the decrease of the fine-structure-splitting interval with increasing angular momentum. For high energies the shapes of the angular distributions from a sequence of states of varying principal quantum number  $n$ , for fixed angular momentum ( $JL$ ), tend to merge into a common curve because at high energies the matrix elements are determined at small distances where all radial wave functions of given ( $JL$ ) have the same shape.

### I. INTRODUCTION

We wish to discuss the influence of relativistic and higher-multipole effects on photoelectron angular distributions from heavy elements as a function of photoelectron energy and of the subshell ( $nJL$ ) from which the electron is removed. There has been increasing interest in these photoelectron angular distributions  $d\sigma/d\Omega$ , particularly within 100 eV above threshold, since they are sensitive to the details of atomic models and dynamics.<sup>1-8</sup> Most work in the past has assumed the validity of nonrelativistic (NR) dipole approximation in which case the unpolarized differential cross section becomes

$$\frac{d\sigma}{d\Omega} = \frac{\sigma_{nL}}{4\pi} \left[ 1 - \frac{1}{2} \beta_{nL} p_2(\cos\theta) \right], \quad (1)$$

characterized by the energy- and subshell-dependent asymmetry parameter  $\beta_{nL}$ , where  $\theta$  is the angle between the momentum vectors of incident photon and ejected photoelectron. For electrons in a central potential, ejected from initial  $s$  states,  $\beta_{no} = 2$ , independent of photoelectron energy, for

in this case the angular distribution in NR dipole approximation is simply proportional to  $\sin^2\theta$ .

However, in various circumstances, important deviations from NR dipole predictions have been noted.<sup>3-8</sup> Walker and Waber<sup>3</sup> worked out the relativistic formalism, which no longer requires that  $\beta_{no} = 2$  in dipole approximation, and other authors<sup>4-8</sup> have recently noted that  $\beta_{no}$  can be quite different from 2 for outer  $s$  shells due to the different radial matrix elements for  $ns \rightarrow \epsilon p_{1/2}$  and  $ns \rightarrow \epsilon p_{3/2}$  transitions which would nonrelativistically be the same.

In a previous work we<sup>9</sup> have also examined the importance of *higher-multipole* as well as relativistic contributions. We found within the central-potential-approximation, experimental results for Ne and Kr in better agreement with our full relativistic multipole calculations than with the NR dipole approximation. In a more general discussion<sup>10</sup> of  $d\sigma/d\Omega$ , making sample calculations for several elements and several subshells, we found that for inner shells, multipole effects were important (except for light elements) down to threshold, while relativistic spin-orbit splitting effects were not important until the energy be-

comes quite high. For outer shells multipole effects were unimportant, while relativistic spin-orbit splitting gave a large deviation from the NR dipole predictions for  $s$  waves, due to the different energies at which the radial matrix elements go through zero and change sign.

Here we wish to report a more systematic study of the deviations of the photoelectron angular distributions from NR dipole predictions, as a function of subshell ( $nJL$ ), for a given high- $Z$  element ( $U$ ,  $Z=92$ ). We will also include some data for other subshells of Hg. As before, we approximate the process as a single electron transition in a screened central potential, which is of course at best only qualitatively useful at low energies, but which seems to indicate the importance of higher-multipole and relativistic effects.

The general relativistic multipole angular distribution of photoelectrons ejected from a given subshell can be written<sup>10,11</sup> (for unpolarized radiation)

$$\frac{d\sigma}{d\Omega} = \frac{\sigma}{4\pi} \sum_{m=0}^{\infty} B_m P_m(\cos\theta), \quad (2)$$

where  $B_0 \equiv 1$ , and where  $-2B_2$  plays the role of  $\beta_{nL}$  in NR dipole theory if all other  $B_m$  except  $B_0$  are small. Here  $\sigma$  is the total cross section for photoemission from the subshell; the coefficients  $B_m$  (energy dependent) of the Legendre polynomials  $P_m$  characterize the angular distribution. The  $B_m$  (as well as  $\sigma$ ) are in turn determined by radial matrix elements, defined by integrals over products of initial and final radial wave functions together with spherical Bessel functions  $j_\lambda(kr)$ , where  $\lambda$  is the photon multipolarity and  $k$  is the photon energy.

In Sec. II we report the results of our calculation of the  $B_m$  for various subshells of uranium and mercury, from near threshold (1 eV) and as high as 100 keV. We identify the circumstances and nature of deviations from NR dipole predictions; for inner shells, relativistic spin-orbit splitting is not important while higher-multipole effects remain large to low energies; for outer  $s$  subshells, spin-orbit splitting of matrix elements to final continuum  $p$  states causes a big deviation from NR dipole behavior while multipole effects are not important. For higher- $L$  states, it is also generally true that higher-multipole effects become smaller for outer shells, while spin-orbit effects decrease with increasing  $L$ . The  $B_2$  for  $L > 0$  oscillate as a function of energy but no qualitative deviation from NR dipole predictions for outer shells was noted in the cases examined here. The remaining subshells of uranium show some more interesting features and will be discussed in our next paper. At very

high energies, for each  $m$  the  $B_m(nJL)$  for a sequence of states of varying principal quantum number  $n$ , for fixed angular momentum  $JL$ , tend to merge into a common energy-dependent curve.

In Sec. III we give expressions for the  $B_m$  in terms of transition matrix elements and phase shifts, focussing on  $B_2$  and, to a lesser extent, on  $B_1$ . For some representative subshells we examine the energy dependence of the dominant matrix elements contributing to these  $B$ 's. We find that relatively simple properties of the matrix elements lead to the more complicated behavior of the  $B_m$ . In particular we see how the existence of two, rather than one, important radial matrix elements in the relativistic outer-shell  $s$  wave case, with somewhat different energy dependences, leads to an angular distribution very different from NR predictions, especially when at least one of the matrix elements goes through zero above threshold (Cooper minimum), as the other matrix element will remain finite at that energy. At higher energies, the matrix elements for a given ( $nJL$ ) subshell are determined at small distances, where all ( $JL$ ) state wave functions have the same shape independent of  $n$ ; the matrix elements for a sequence of such subshells of fixed  $J, L$  but varied  $n$  will have the same photoelectron energy dependence for energies which are large compared to subshell binding energies. As a result, for each  $m$  the sequence of  $B_m$  as  $n$  varies for fixed ( $JL$ ) tends to merge into a common curve as the energy becomes higher. Inner-shell  $B_m$  reach the common curve only at the highest energies, both because inner-shell wave functions, due to their larger binding energies, deviate from a common shape at smaller distances, and because when we pick a given energy (and wave function) for the outgoing photoelectron, the photon energies (and wave function) differ more for inner shells at low energies. For outer subshells of higher angular momentum (Hg  $5d_{5/2}$ , U  $6p_{3/2}$ , and U  $4f_{7/2}$ ) we see only small higher-multipole effects until the photoelectron energy becomes as high as 1 keV. The resulting angular distribution of an outer  $d$  subshell (Hg  $5d_{5/2}$ ) shows the same oscillating feature as Manson found in an NR dipole calculation.<sup>1,12</sup> We have also examined for various  $s$  states of uranium the matrix elements and the phase-shift differences contributing to  $B_1$ , which characterize the first higher-multipole effects beyond dipole approximation.

## II. PHOTOELECTRON ANGULAR DISTRIBUTIONS FOR URANIUM AND MERCURY

We present in Figs. 1–5,  $B_1$  through  $B_4$  for all  $K, L$ , and  $N$  subshells and some  $M, O, P$ , and  $Q$  subshells of uranium, as well as for several

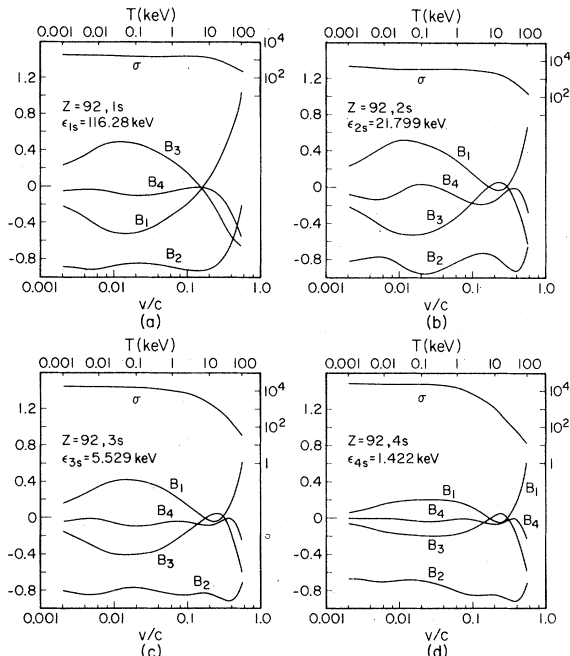


FIG. 1. Total cross sections (top curve and right-hand scale in barns) and  $B_m$  coefficients (lower curves and left-hand scale in dimensionless units) for  $m=1-4$ , of uranium 1-4s subshells. Lower horizontal scale is outgoing electron velocity  $v/c$ , with the corresponding electron kinetic energy  $T$  in keV on the top horizontal scale.

outer subshells of mercury, as a function of the outgoing photoelectron velocity  $v/c$  (or kinetic energy  $T$ ). The uranium cases include photoeffects from all  $s$  states and selected  $p$ ,  $d$ , and  $f$  states as shown in Table I. In each of the figures we also show (on a separate scale) the corresponding total cross section for the subshell. We note that it is possible to have significant variations in the angular distributions in an energy range through which the total cross section is essentially constant. As we had observed before,<sup>10</sup> the total cross sections are roughly constant until the continuum electron kinetic energy (top scale of each figure) becomes comparable with the binding energy of the initial electron, except for cases in which a shape resonance occurs. In all the figures we see that the  $B_m$  generally grow rapidly at high energy, reflecting the increasing forward peaking of the angular distribution, characterized by features such as  $[1 - (v/c) \cos\theta]^{-4}$  and so by large coefficients in a Legendre polynomial expansion.

Figure 1 shows photoeffect angular distribution coefficients from 1s-4s subshells of uranium, and we notice that  $B_1$  ( $\cong -B_3$ ) grows much larger at low energies as we go into the inner shells, indicating that higher-multipole effects are im-

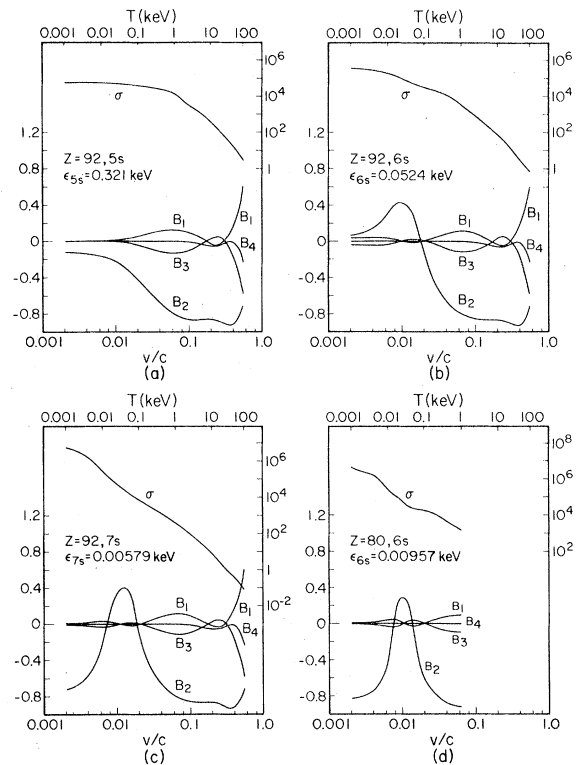


FIG. 2. The same as Fig. 1, for U 5-7s subshells and the Hg 6s subshell.

portant for inner-shell photoeffect down to threshold.  $B_1$  for the 1s state is qualitatively different in behavior from all the others, remaining large and negative for photoelectron energies from threshold to 10 keV.  $B_2$  remains fairly close to the NR dipole value of  $-1$ . In Fig. 2 we show the 5s, 6s, and 7s subshells of uranium and the 6s subshell of mercury. Here we see quite different features from those of Fig. 1. While  $B_1 \cong -B_3$  becomes smaller as we proceed into the outer shells and is negligible at low energies,  $B_2$  shows a drastic change from the NR dipole value of  $-1$ . In U 5s,  $B_2$  becomes small at threshold, while in 6s,  $B_2$  goes through zero and changes sign at about 90 eV above threshold, then approaching zero from above. In U 7s and Hg 6s we see at energies lower than 100 eV two sign changes over a relatively small energy range, above and below which  $B_2$  returns nearly to the NR dipole value. We will discuss the origin of this feature in terms of matrix elements in Sec. III; however, we may already note that in this last case the total cross section shows some hint of a Cooper minimum in the region where  $B_2$  is rapidly varying. This suggests that the different positions of the zeros of the two relativistic matrix elements cause qualitatively different features in the resulting angular

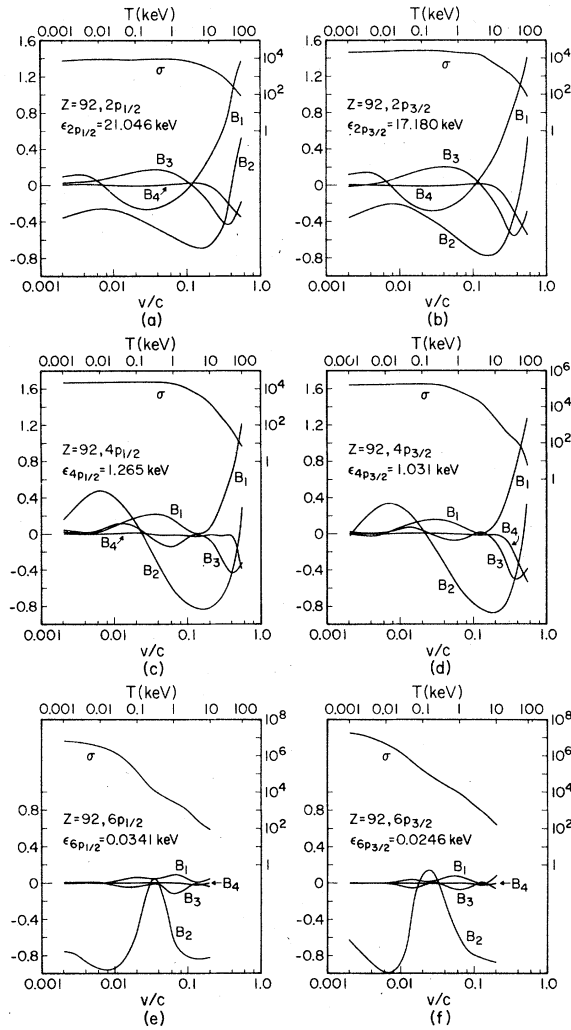


FIG. 3. The same as Fig. 1, for U  $2p$ ,  $4p$ , and  $6p$  subshells.

distributions from the NR distributions (determined by a single matrix element).

Figure 3 shows  $l=1$  states of the  $L$ ,  $N$ , and  $P$  shells of uranium. We see a bigger difference between  $6P_{1/2}$  and  $6P_{3/2}$  subshell photoelectron angular distribution parameters than for the more inner  $p$  shells, while as before, multipole effects are larger for inner shells. We again note that, as for  $1s$ , for innermost  $P$  subshells ( $2P_{1/2}$  and  $2P_{3/2}$ )  $B_1$  becomes negative at intermediate energies (approximately 10 eV–10 keV).

Figure 4 shows the  $l=2$  states of the  $N$  and  $P$  shells of uranium and the  $O$  shell of mercury, while the first two panels of Fig. 5 give the U  $4f_{5/2}$  and  $4f_{7/2}$  cases. We observe that for higher-orbital angular-momentum states  $B_2$  oscillates more with energy, as has also been seen in some nonrelativistic calculations. Manson<sup>1,12</sup>,

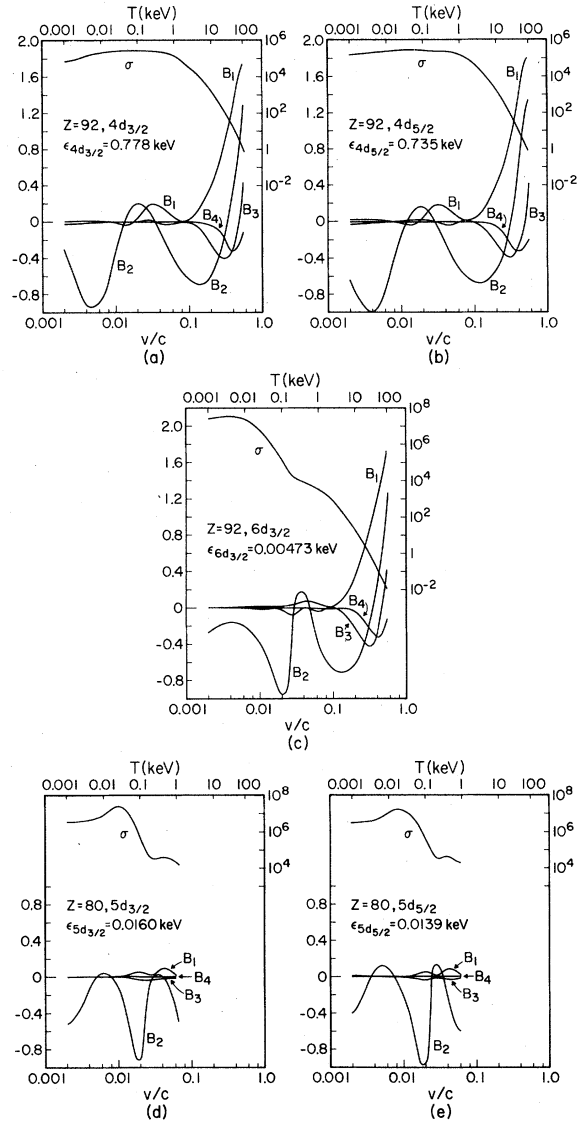


FIG. 4. The same as Fig. 1, for U  $4d$ , U  $6d_{3/2}$ , and Hg  $5d$  subshells.

for example, observed the same oscillatory feature in his NR dipole calculation for Xe  $4d$  subshell, as we observe in U  $6d_{3/2}$ , Hg  $5d_{3/2}$ , and Hg  $5d_{5/2}$  subshells; he identified three origins for the oscillations which we will discuss in Sec. III.

Finally, we note from the last two panels of Fig. 5 that for high energies,  $B_1$  and  $B_2$  for most  $s$  states have similar energy dependences. For the  $1s$  state  $B_1$  and  $B_2$  deviate even at the highest energies shown from  $B_1$  and  $B_2$  of the other states (due, as we discuss in Sec. III, to the much larger binding energy). The  $2s$  state starts to deviate from the common curves next, then  $3s$ , and so on. Large negative values of  $B_1$  ( $\cong -B_3$ ) for the  $1s$  state in contrast with all the other  $s$  shells

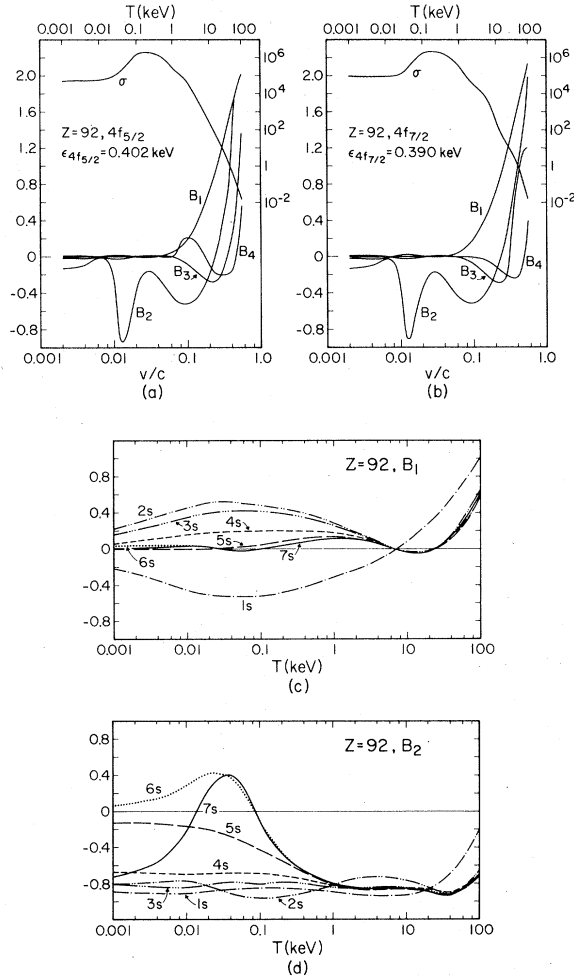


FIG. 5. (a) and (b) The same as Fig. 1, for U  $4f$  subshells. (c)  $B_1$  for 1–7s subshells of uranium, superimposed in one graph as functions of outgoing electron kinetic energy  $T$ . (d) The same as (c) for  $B_2$ .

TABLE I. Summary of subshell cases examined in this work.

$Z = 92$ (U)	
K	$1s_{1/2}$
L	$2s_{1/2}; 2p_{1/2}, 2p_{3/2}$
M	$3s_{1/2}; ---, ---; ---, ---$
N	$4s_{1/2}; 4p_{1/2}, 4p_{3/2}; 4d_{3/2}, 4d_{5/2}; 4f_{5/2}, 4f_{7/2}$
O	$5s_{1/2}; ---, ---; ---, ---; ---, ---$
P	$6s_{1/2}; 6p_{1/2}, 6p_{3/2}; 6d_{3/2}$
Q	$7s_{1/2}$
$Z = 80$ (Hg)	
O	$---; ---, ---; 5d_{3/2}, 5d_{5/2}$
P	$6s_{1/2}$

throughout most of the energy regions shown, imply that the  $K$ -shell distribution is significantly backward peaked.

### III. MATRIX ELEMENTS

The  $B_m$  are directly related to the experimentally observable angular distributions, while in a theoretical calculation the  $B_m$  can be determined from radial matrix elements, which are less directly observable. We will see, however, that the relatively complicated properties of the  $B_m$  result from rather simple properties of matrix elements. We know that

$$\begin{aligned} d\sigma/d\Omega &= \left(\frac{\sigma}{4\pi}\right) \sum B_m P_m(\cos\theta) \\ &= (2\pi)^{-2} p E |M_{fi}|^2, \end{aligned} \quad (3)$$

where  $E \equiv 1 + T$  is the total energy (including rest-mass energy and subject to the energy conservation) of the photoelectron,  $p$  the magnitude of its momentum, and

$$M_{fi} = \left(\frac{2\pi\alpha}{k}\right)^{1/2} \int \psi_f^\dagger \vec{\alpha} \cdot \vec{\epsilon} e^{i\vec{k}\cdot\vec{r}} \psi_i d^3r, \quad (4)$$

for photon energy and momentum  $k$  and  $\vec{k}$ , respectively, with polarization  $\vec{\epsilon}$ . (We are using dimensionless units  $\hbar = c = m_e = 1$  and  $\alpha =$  fine-structure constant  $\cong \frac{1}{137}$  and

$$\vec{\alpha} = \begin{pmatrix} 0 & \vec{\sigma} \\ \vec{\sigma} & 0 \end{pmatrix}$$

with  $\vec{\sigma} \times 2 \times 2$  Pauli matrices.) Equation (4) reduces in the NR limit to

$$M_{fi} = \left(\frac{2\pi\alpha}{k}\right)^{1/2} \int \psi_f^* \vec{p} \cdot \vec{\epsilon} e^{i\vec{k}\cdot\vec{r}} \psi_i d^3r, \quad (5)$$

with single-component Schrödinger wave functions  $\psi$  replacing the 4-component wave functions  $\psi$  of Eq. (4). This further reduces in NR dipole approximation to

$$\begin{aligned} M_{fi} &= \left(\frac{2\pi\alpha}{k}\right)^{1/2} \int \psi_f^* \vec{p} \cdot \vec{\epsilon} \psi_i d^3r \\ &= i(2\pi\alpha k)^{1/2} \int \psi_f^* \vec{r} \cdot \vec{\epsilon} \psi_i d^3r. \end{aligned} \quad (6)$$

The general expression for the  $B_m$  in terms of relativistic multipole matrix elements and phase-shift differences, resulting from an expansion in partial waves, has been given in our review of atomic photoeffect<sup>11</sup>; we shall not repeat this rather complicated expression here. In relativistic dipole approximation the expression reduces,<sup>3</sup> after averaged over initial polarizations and summed over initial and final electron states, to

$$\begin{aligned}
B_m = & A \sum_{\kappa \bar{\kappa}} (-1)^{J+1/2} \cos[\delta_\kappa - \delta_{\bar{\kappa}} + \frac{1}{2}\pi(\bar{l}-l)] \\
& \times (2j+1)(2\bar{j}+1)(2m+1) \begin{pmatrix} j & \bar{j} & m \\ \frac{1}{2} & -\frac{1}{2} & 0 \end{pmatrix} \\
& \times W(11\bar{j}\bar{j}; mJ) \begin{pmatrix} 1 & 1 & m \\ 1 & -1 & 0 \end{pmatrix} \frac{2J+1}{16\pi} \\
& \times \begin{pmatrix} j & J & 1 \\ \frac{1}{2} & -\frac{1}{2} & 0 \end{pmatrix} \begin{pmatrix} \bar{j} & J & 1 \\ \frac{1}{2} & -\frac{1}{2} & 0 \end{pmatrix} R_j R_{\bar{j}}, \quad (7)
\end{aligned}$$

if  $l+\bar{l}+m$  is even ( $B_m=0$  otherwise), where

$$\begin{aligned}
\frac{1}{A} = & \frac{2J+1}{16\pi} \left( \frac{2J-1}{12J} R_{J-1}^2 + \frac{1}{12J(J+1)} R_J^2 \right. \\
& \left. + \frac{2J+3}{12(J+1)} R_{J+1}^2 \right) \\
= & (k/64\pi^2 \alpha p E) \sigma, \quad (8)
\end{aligned}$$

so that  $B_0 \equiv 1$  (notice that  $B_0 = \sigma/4\pi$  in our review since the  $B_m$  are defined there by  $d\sigma/d\Omega = \sum B_m P_m$ ). Also

$$\begin{aligned}
R_j \equiv & (\kappa - K + 1) \int G_K j_\sigma f_\kappa dr \\
& + (\kappa - K - 1) \int F_K j_\sigma g_\kappa dr, \quad (9)
\end{aligned}$$

where  $G$ ,  $F$  and  $g$ ,  $f$  are the large and small components of Dirac electron wave functions of bound

and continuum states, respectively; the  $\delta$ 's are the corresponding phase shifts for the two final continuum states characterized by  $\kappa$  and  $\bar{\kappa}$ , and  $K$  and  $\kappa$  are the quantum numbers combining angular momentum and parity for bound and continuum states, respectively. [ $\kappa = (-1)^{j+1/2}(j+\frac{1}{2})$ .] In the NR limit the large components  $G$  and  $g$  reduce to the NR radial wave functions, while the small components  $F$  and  $f$  become<sup>3</sup>

$$F \rightarrow \frac{1}{2} \left( \frac{d}{dr} + \frac{K}{r} \right) G, \quad f \rightarrow \frac{1}{2} \left( \frac{d}{dr} + \frac{\kappa}{r} \right) g. \quad (10)$$

In this limit Eq. (9) reduces to the NR equivalents of the dipole velocity form

$$\begin{aligned}
R_{L+1} = & \int_0^\infty p_{e, L+1}^*(r) \left( \mp \frac{d}{dr} + \frac{2L+1 \pm 1}{2r} \right) P_{nL}(r) dr \\
= & k \int_0^\infty p_{e, L+1}^*(r) r P_{nL}(r) dr, \quad (11)
\end{aligned}$$

if the continuum and discrete radial wave functions  $p_{e1}/r$  and  $P_{nL}/r$ , respectively, are exact. Here,

$$\begin{aligned}
R_{J-1} = & \begin{cases} R_J = -R_{L-1}, & \text{if } K > 0 \quad (J = L - \frac{1}{2}) \\ R_{L-1}, & \text{if } K < 0 \quad (J = L + \frac{1}{2}) \end{cases} \\
R_{J+1} = & \begin{cases} R_{L+1}, & \text{if } K > 0 \quad (J = L - \frac{1}{2}) \\ R_J = R_{L+1}, & \text{if } K < 0 \quad (J = L + \frac{1}{2}). \end{cases} \quad (12)
\end{aligned}$$

From Eqs. (7) and (8),  $B_0 \equiv 1$  and

$$\begin{aligned}
B_2 = & -\frac{(2J+1)}{32\pi} A \left( \frac{(2J-3)(2J-1)}{48J^2} R_{J-1}^2 - \frac{(2J-1)(2J+3)}{48J^2(J+1)^2} R_J^2 + \frac{(2J+3)(2J+5)}{48(J+1)^2} R_{J+1}^2 \right. \\
& \left. + \frac{2J-1}{8J^2(J+1)} \text{Re}(\bar{R}_J \bar{R}_{J-1}^*) + \frac{(2J+3)}{8J(J+1)^2} \text{Re}(\bar{R}_J \bar{R}_{J+1}^*) + \frac{(2J+1)(2J+3)}{8J(J+1)} \text{Re}(\bar{R}_{J-1} \bar{R}_{J+1}^*) \right), \quad (13)
\end{aligned}$$

while other  $B_m=0$ ; thus, in general, *three* radial matrix elements contribute to the cross section and angular distributions within relativistic dipole approximation. Here,  $\bar{R}_j = R_j e^{i\delta_j}$ .

For bound  $s$  states, only  $R_{1/2}$  and  $R_{3/2}$  contribute in relativistic dipole approximation. These two matrix elements characterize  $ns \rightarrow \epsilon p_{1/2}$  and  $ns \rightarrow \epsilon p_{3/2}$  transitions, respectively,

$$B_2 = -\frac{R_{3/2}^2 + 2R_{3/2}R_{1/2} \cos(\delta_{-2} - \delta_1)}{R_{1/2}^2 + 2R_{3/2}^2}. \quad (14)$$

Nonrelativistically,  $R_{3/2} = R_{1/2}$  and  $\delta_{-2} = \delta_1$  so that  $B_2$  reduces to  $-1$ . We have found that the cosine of the phase-shift difference  $\delta_{-2} - \delta_1$  between the

two continuum states  $\epsilon p_{1/2}$  and  $\epsilon p_{3/2}$  for uranium is fairly constant, close to 0.9, over the entire energy region considered in this work. This indicates that the spin-orbit effect has little energy dependence. Thus when the ratio of the two matrix elements  $R_{3/2}/R_{1/2}$  for the given  $ns$  subshell is close to 1 (the NR ratio), we get  $B_2$  close to  $-1$  (the NR value). But if either matrix element vanishes for some energy at which the other matrix element has a nonzero value, the ratio will be very different from 1 and hence  $B_2$  will be very different from  $-1$ . These circumstances arise when the matrix elements change sign above threshold. When  $R_{3/2} = 0$ ,  $B_2 = 0$ .  $B_2$  has its maximum value, which in the case of equal phases  $\delta_{-2} = \delta_1$  is

+0.5, achieved for  $R_{3/2} = -0.5 R_{1/2}$ ; for the equal-phase case it returns to 0 by  $R_{3/2} = -2 R_{1/2}$  and by  $R_{1/2} = 0$ ,  $B_2$  has become  $-0.5$ .

Figure 6 shows the energy dependence of  $p R_{1/2}/N_{ns}$  and  $p R_{3/2}/N_{ns}$  for the 1s, 3s, 5s, 6s, and 7s states, where each  $R$  is divided by the normalization constant  $N_{ns}$  for the  $ns$  bound states. Since we have multiplied  $R$  by  $p$ , the momentum of the photoelectron, we do not see the divergence of  $R$ 's near threshold. This exhibits the common features in these curves, for reasons we shall discuss subsequently. As previously remarked, we see that for all  $n$  these reduced  $ns$  matrix elements of given  $(JL)$  merge into a common curve as energy increases. We can also see that the large deviation from the NR dipole prediction for  $B_2$  [Fig. 5(d)], which occurs for outer shells at lower energies, is due to the different (shifted) positions of the zeros of  $R_{1/2}$  and  $R_{3/2}$ , which would coincide in NR dipole approximation. In this NR limit the cross section vanishes as the matrix elements pass through zero at the Cooper minimum, but the angular distribution shape does not change through this region. [We have divided the  $R$ 's by  $N_{ns}$  in order to exhibit the common energy dependence at high energy, but it should be realized that, contrary to the casual impression from Fig. 6, the  $R$ 's themselves become *smaller* with increasing  $n$ . Threshold cross sections do tend to

increase with  $n$ , since as the threshold energy decreases,  $k^{-1/2}$  in Eq. (4) usually grows faster than the  $R$ 's decrease.]

Comparing Fig. 5(d) and Fig. 6, we see that the matrix elements do not vanish above threshold for inner shells (as for the 1s and 3s cases shown in Fig. 6) and so  $B_2$  remains close to  $-1$ . This behavior persists until 5s, where  $R_{3/2}$  has nearly vanished by threshold, so that  $B_2$  deviates substantially from  $-1$  (approaching 0) at threshold. For 6s  $R_{3/2}$  has passed through 0 above threshold, allowing  $B_2 \cong 0.4$  (0.28 for Hg 6s) at its maximum (rather than 0.5 which we would get if  $\delta_{3/2} = \delta_{1/2}$ ), but  $-R_{3/2}$  is not yet bigger than  $2R_{1/2}$  by threshold, so that  $B_2$  does not return to negative values. By 7s, both  $R$ 's have gone through 0 above threshold, so that after the peak value of  $B_2 \cong 0.4$ ,  $B_2$  has returned to  $-0.72$  by threshold. We see in Fig. 5(d) a minimum in  $B_2$  of about  $-0.9$  for all  $s$  subshells of uranium except 1s at approximately 40 keV photoelectron energy; Figure 6 shows that this feature arises because at this energy the common  $R_{1/2}$  and  $R_{3/2}$  curves of uranium  $s$  states cross over ( $R_{1/2} = R_{3/2}$ ) so that  $B_2$  would become  $-1$  if  $\delta_{3/2} = \delta_{1/2}$ . (The position of the minimum is somewhat shifted from the matrix element crossover since the phase shifts are not equal.) The 1s matrix elements do not cross over in the dipole regime and so we do not see such a feature in  $B_2$  for the 1s case.

We have noted that for high energies,  $B_1$ ,  $B_2$  [Figs. 5(c) and 5(d)] and  $R$ 's (Fig. 6) for most  $s$  states have similar energy dependences; the same property is found for the  $n$  dependence of any fixed  $(JL)$ . The property of  $s$  state cases reflects the fact that at high energies the matrix element for a given subshell is determined at rather small distances, where, apart from normalization, all  $s$ -state wave functions have the same shape; similar comparisons can be made among  $p$  states, etc. Such a common shape is the shape of a near-zero-energy bound or continuum wave function of given  $(JL)$ . The greater the energy (positive or negative) of a state, the smaller is this distance at which its wave function deviates from this common shape. An inner-shell bound-state wave function deviates within its orbit. The matrix element for a subshell is determined within the region of common wave function shape if the photon energy is several times the threshold photon energy for ionization of that subshell. (For the uranium 1s state, the highest energy which we have displayed is still not high enough to be well above the 1s threshold.) Normalizations and hence the absolute cross sections, of course do depend on the principal quantum number  $n$ . As we approach lower photoelectron energies, the photon

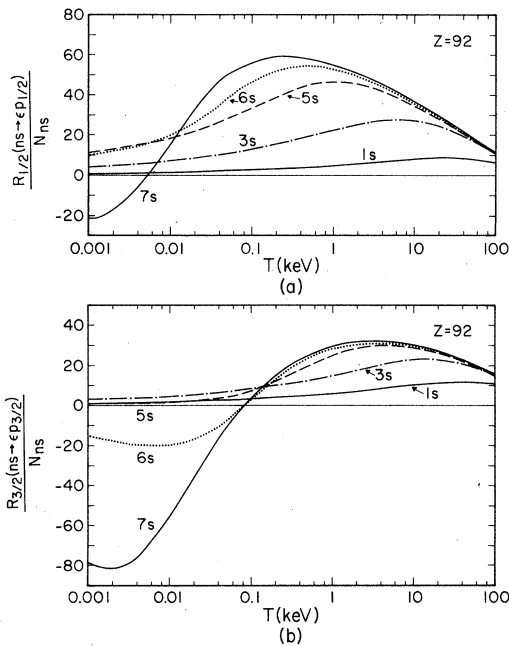


FIG. 6. Dipole transition matrix elements  $R_i$  from  $U ns$  to  $\epsilon p_i$ , divided by bound-state normalizations  $N_{ns}$  and multiplied by momentum  $p$  of the photoelectrons in arbitrary units. (a)  $R_{1/2}(U ns \rightarrow \epsilon p_{1/2})$ . (b)  $R_{3/2}(U ns \rightarrow \epsilon p_{3/2})$ .

energy for each given inner shell successively ceases to be well above its ionization threshold; the matrix element for such a subshell begins to be determined at larger distances, where the bound-state wave function for that subshell has already deviated from the common shape. Hence the character of the  $B_m$  for such a subshell begins to deviate from the common curves describing those shells exterior to the given shell.

In general, spin-orbit effects become smaller as angular momentum increases. For  $J=L \pm \frac{1}{2}$  initial bound states of outer shells, where multipole effects are small and where except for  $L=0$  there are two nonrelativistic radial matrix elements, one of which will split into two when spin-orbit interaction is added. The resulting photoelectron angular distributions for  $L>0$  cases which we observe here are not qualitatively different from those obtained in NR dipole calculations. (Quantitative differences, and energy shifts, between  $J=L \pm \frac{1}{2}$  distributions remain noticeable.) Manson<sup>1,12</sup> observed the same oscillating features in his NR

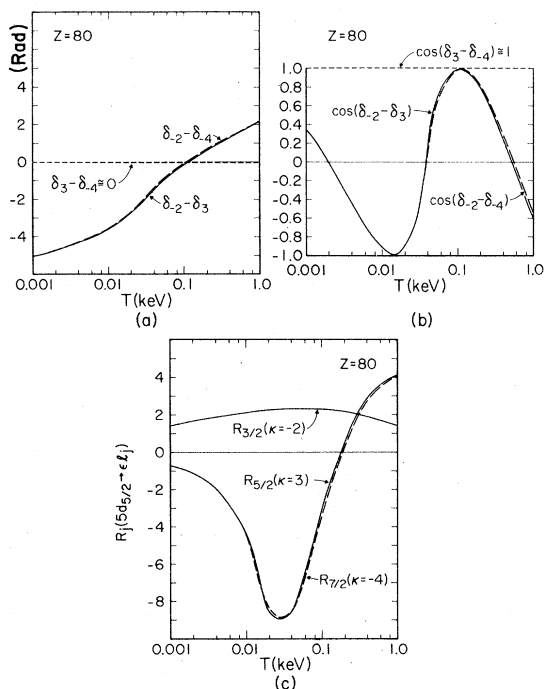


FIG. 7. (a) Phase-shift differences between the three final continuum states  $\kappa = -2(\epsilon p_{3/2})$ ,  $\kappa = 3(\epsilon f_{5/2})$ , and  $\kappa = -4(\epsilon f_{7/2})$  relevant for the calculation of mercury  $5d_{5/2}$  photoeffect in relativistic dipole approximation, demonstrating that  $\delta_3$  and  $\delta_4$  have a significant energy dependence. (b) Cosines of the phase differences of (a). (c) Dipole transition matrix elements  $R_j$  ( $\text{Hg } 5d_{5/2} \rightarrow \epsilon l_j$ ) multiplied by momentum  $p$  of photoelectron, in arbitrary units, showing a Cooper minimum above a shape resonance for  $R_{7/2}$  and  $R_{5/2}$ .

dipole calculation for the Xe  $4d$  subshell as we observe for U  $6d_{3/2}$ , Hg  $5d_{3/2}$ , and Hg  $5d_{5/2}$  subshells. He identified three origins for these oscillations of the asymmetry parameter: a Cooper minimum, below it a shape resonance, and finally, just above the threshold (below the range of our calculation), a Coulomb phase-shift change. Our total cross sections in Fig. 4 do indeed show shape resonances and Cooper minima features at the positions of these oscillations in  $B_2$ , in agreement with his analysis. To demonstrate this more clearly we show in Fig. 7 the phase-shift differences (and their cosines) and radial matrix elements for Hg in the  $5d_{5/2}$  case, corresponding to Fig. 4(e). We see that the relevant phase-shift difference rapidly changes by  $\pi$  (corresponding to a rapid variation of  $\delta_{-3} \approx \delta_4$ ), with a shape resonance in the matrix elements at the same energy. This is followed by a zero (Cooper minimum) in the same radial matrix elements at a higher energy. We do not see any qualitative relativistic effects, due to the small spin-orbit effects on  $\epsilon f_{5/2}$  and  $\epsilon f_{7/2}$  states, which as we show leads to almost the same matrix elements for  $5d_{5/2} \rightarrow \epsilon f_{5/2}$  and  $5d_{5/2} \rightarrow \epsilon f_{7/2}$  transitions.

For outer  $p$  and  $f$  subshells, the situation is somewhat similar. However, in Fig. 8 we see

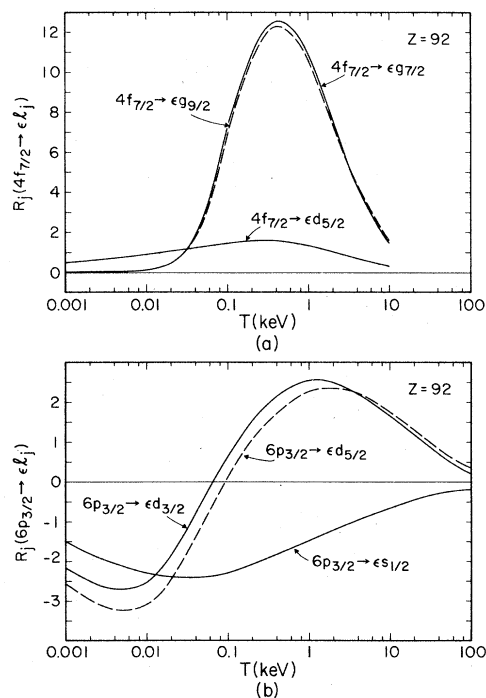


FIG. 8. The same as Fig. 7(c). (a) for  $R_j(\text{U } 4f_{7/2} \rightarrow \epsilon l_j)$ , showing shape resonances and Cooper minima probably just below the threshold. (b) For  $R_j(\text{U } 6p_{3/2} \rightarrow \epsilon l_j)$ , with less obvious shape resonances and a little larger separation between zeros.

in the uranium  $4f_{7/2}$  subshell a shape resonance at higher energies with a Cooper minimum probably below threshold, while for the uranium  $6p_{3/2}$  substate the separation of zeros of matrix elements is a little larger and a shape resonance is less obvious.

Finally, we may discuss the radial matrix elements which are responsible for higher-multipole contributions, limiting our attention to emission from  $s$  states. To characterize the full relativistic transition matrix elements from a given  $(JL)$  state

to a final continuum state specified by  $j$  and  $l$  due to a photon of multipolarity  $\lambda$ , via a  $2^\lambda$ -pole transition, we adopt the notation

$$(\Lambda \lambda 2j l) \equiv (\kappa - K + \Lambda) \int G_{Kj\lambda} f_{\kappa} dr + (\kappa - K - \Lambda) \int F_{Kj\lambda} g_{\kappa} dr. \quad (15)$$

Then we have for emission from  $s$  states, keeping the leading terms only,

$$B_1 = \frac{9}{25} [5(1011)(2132) \cos(\delta_1 - \delta_2) + (1031)(2132) \cos(\delta_{-2} - \delta_2) + 9(1031)(2152) \cos(\delta_{-2} - \delta_{-3})] / [(1011)^2 + 2(1031)^2]. \quad (16)$$

In this notation,  $R_{1/2} = (1011)$  and  $R_{3/2} = (1031)$ . The additional radial matrix elements which enter this expression, (2132) and (2152), are shown in Fig. 9(a) for the  $s$  states of uranium, again divided by the corresponding bound-state normalizations.

The merging of these additional matrix elements, except  $1s$ , in the same fashion as for  $R_{1/2}$  and  $R_{3/2}$ , explains the common high-energy  $B_1$  curve for the uranium  $s$  shells; the merging is again to be understood in terms of the determination of these matrix elements at small distances. In the NR limit,

$$B_1 = \frac{27}{5} R_p Q_d \cos(\delta_p - \delta_d) / R_p^2,$$

for  $s$  waves, where  $R_p = R_1$  for  $K = -1$  in Eq. (12), and  $Q_d$  is the matrix element for  $ns \rightarrow \epsilon d$  electric quadrupole transition.

Figure 9(b) shows the cosines of the three phase-shift differences of Eq. (16). We see that  $\cos(\delta_{-2} - \delta_{-3})$  and  $\cos(\delta_{-2} - \delta_2)$  are closer to each other than to  $\cos(\delta_1 - \delta_2)$ , indicating that the difference in phase shift due to spin-orbit coupling is larger between  $\epsilon p_{1/2}$  ( $\kappa = 1$ ) and  $\epsilon p_{3/2}$  ( $\kappa = -2$ ) than between  $\epsilon d_{3/2}$  ( $\kappa = 2$ ) and  $\epsilon d_{5/2}$  ( $\kappa = -3$ ). [In fact,  $\cos(\delta_1 - \delta_{-2})$  is close to 0.90 over the entire energy range with fluctuation of  $\pm 0.01$ , and  $\cos(\delta_2 - \delta_{-3})$  is within  $0.995 \pm 0.005$ . At the highest energy shown, the deviations of these two cosines from 1 become slightly bigger.] From Figs. 6 and 9, we can explain the common zeros in  $B_1$  in the high-energy region of Fig. 5(c). For photoelectron energies of about 25 keV, all three cosines in Fig. 10 and all the dipole matrix elements in Fig. 6 are nonzero, but all the quadrupole matrix elements in Fig. 9 except for the  $1s$  case go through zero, resulting in the common zero in  $B_1$  for all  $ns$  states (except for  $1s$ ) at around 25 keV in Fig. 5(c). Between 4 and 10 keV, none of the matrix elements in Eq. (15) are zero but the first term in Eq. (15) is opposite in sign to the other terms

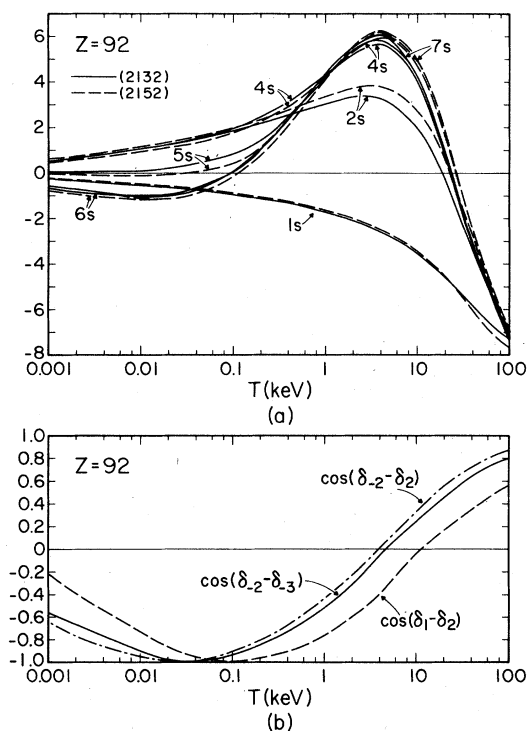


FIG. 9. (a) Quadrupole transition matrix elements (2132)—and (2152)—, contributing to  $B_1$ , for  $U ns$ ,  $n=1, 2, 4, 5, 6, 7$ , scaled as in Fig. 6. (b) The cosines of the phase-shift differences contributing to  $B_1$ .

due to the cosines, as we see in Fig. 9(b). This negative contribution will cancel the positive contribution somewhere between 4 and 10 keV, because  $(2132) \cong (2152)$  and  $(1011)$  and  $(1031)$  are comparable to each other for all  $ns$  states. The resulting zeros in  $B_1$  are at about 7 keV for all  $ns$  states.

## ACKNOWLEDGMENTS

This research was supported in part by the National Science Foundation of the United States of America under Grants Nos. PHY-78-26491 and INT-79-00982, and in part by the National Science Council of the Republic of China.

<sup>1</sup>D. J. Kennedy and S. T. Manson, Phys. Rev. A 5, 227 (1972).

<sup>2</sup>M. Ya. Amusia, N. A. Cherepkov, and L. V. Chernysheva, Phys. Lett. A40, 15 (1972).

<sup>3</sup>T. E. H. Walker and J. T. Waber, J. Phys. B 6, 1165 (1973); 7, 674 (1974).

<sup>4</sup>N. A. Cherepkov, Phys. Lett. A66, 204 (1978).

<sup>5</sup>W. R. Johnson and K. T. Cheng, Phys. Rev. Lett. 40, 1167 (1978); Phys. Rev. A 20, 978 (1979).

<sup>6</sup>W. Ong and S. T. Manson, Phys. Rev. A 19, 688 (1979); 20, 2364 (1979).

<sup>7</sup>M. G. White, S. H. Southworth, P. Kobrin, E. D. Po-

liakoff, R. A. Rosenberg, and D. A. Shirley, Phys. Rev. Lett. 43, 1661 (1979).

<sup>8</sup>S. T. Manson and A. F. Starace, Bull. Am. Phys. Soc. 24, 1175 (1979).

<sup>9</sup>Akiva Ron, R. H. Pratt, and H. K. Tseng, Chem. Phys. Lett. 47, 377 (1977).

<sup>10</sup>H. K. Tseng, R. H. Pratt, Simon Yu, and Akiva Ron, Phys. Rev. A 17, 1061 (1978).

<sup>11</sup>R. H. Pratt, Akiva Ron, and H. K. Tseng, Rev. Mod. Phys. 45, 273 (1973). We are following the notation of this review paper.

<sup>12</sup>S. T. Manson, Phys. Rev. Lett. 26, 219 (1971).